Applied Radiation and Isotopes 226 (2025) 112171

Contents lists available at ScienceDirect

Applied Radiation and Isotopes

journal homepage: www.elsevier.com/locate/apradiso

Assessment of scintigraphic imaging with Terbium-161: A visual and quantitative analysis

Florian Rosar [a,*], Sven Petto [a], Sebastian Ganz [a], Caroline Burgard [a], Stephan Maus [a], Mark Bartholomä [a], Isabelle Miederer [b], Mathias Schreckenberger [b], Samer Ezziddin [a], Andrea Schaefer-Schuler [a]

[a] Dept. of Nuclear Medicine, Saarland University, Homburg, Germany
[b] Dept. of Nuclear Medicine, Johannes Gutenberg-University, Mainz, Germany

ARTICLE INFO

Keywords:
^{161}Tb
Tb-161
SPECT
Quantification
Phantom measurement

ABSTRACT

The Auger emitter ^{161}Tb is an increasingly discussed radionuclide for targeted radionuclide therapy. The aim of this study was to assess the feasibility of scintigraphic imaging with ^{161}Tb in terms of image quality and quantitative capabilities by phantom measurements and to evaluate the suitability of this radionuclide for clinical use. Phantom measurements were conducted using a standardized NEMA IEC body phantom filled with activity concentrations ranging from 2.5 GBq to 100 MBq. Both visual and quantitative analyses were performed, including assessment of the image calibration factor (CF), as well as the recovery coefficient (RC) and the contrast-to-noise ratio (CNR) of the individual spheres. The results observed in this study demonstrate that quantitative SPECT/CT imaging with ^{161}Tb is feasible over a wide range of activity making this radionuclide suitable for clinical applications. Acquiring a total of at least 5 million photopeak counts enables visual detectability of lesions of diameter lower than 20 mm and quantitative calibration for dosimetry purposes.

1. Introduction

The development and implementation of targeted radionuclide therapies, such as prostate-specific membrane antigen (PSMA)-targeted radioligand therapy (RLT) or peptide receptor radionuclide therapy (PRRT), has revolutionized nuclear medicine treatment options for prostate cancer and neuroendocrine tumors (Sartor et al., 2021; Strosberg et al., 2017). Currently, the radionuclide Lutetium-177 (^{177}Lu) is the standard for both therapies, typically in the form of [^{177}Lu]Lu-PSMA-617 or [^{177}Lu]Lu-DOTATATE, which both were approved by the FDA and EMA in recent years (Kratochwil et al., 2023; Love et al., 2022). To further enhance the effectiveness of the therapy, new approaches, such as the use of other radionuclides as an alternative to ^{177}Lu, e.g., Terbium-161 (^{161}Tb), are being intensively discussed (Müller et al., 2023; Al-Ibraheem and Scott, 2023).

^{161}Tb has similar physical decay characteristics to the established ^{177}Lu. Common features of both radionuclides (^{161}Tb vs. ^{177}Lu) include a similar half-life (6.906 days vs. 6.647 days) and the emission of β^- particles with similar energy (average energy 154 keV vs. 133 keV) (Champion et al., 2016). Additionally, both radionuclides emit γ-rays which can be used for scintigraphic imaging (for ^{161}Tb mainly 74.6 keV and 48.9 keV with emission probabilities of 10.2 % and 17.0 % and for ^{177}Lu mainly 208 keV and 113 keV with emission probabilities of 10.4 % and 6.6 %, respectively).

In comparison to ^{177}Lu, a larger number of low-energy Auger (AE) and conversion electrons (CE) are emitted during the ^{161}Tb beta decay process with very short ranges in tissue (0.5–30 μm). According to recent scientific reports and calculations, these low energy electrons (electron energy range: AE 0.018–50.9 keV; CE 3.3–98.3 keV) provide higher local dose density and therefore higher absorbed radiation dose in tumors, potentially increasing therapeutic effectiveness (Hindié et al., 2016; Alcocer-Ávila et al., 2020; Verburg et al., 2023; Schaefer-Schuler et al., 2024). This could offer important advantages, especially in the treatment of micrometastases. Preclinical studies have indicated the therapeutic superiority of ^{161}Tb over ^{177}Lu in cell experiments (Müller et al., 2014, 2019; Grünberg et al., 2014; Borgna et al., 2022). It should be noted, however, that changing the radionuclide not only alters the physical properties of the tracer but can also affect its biochemical profile (Reubi et al., 2000). In addition, the feasibility of clinical translation of ^{161}Tb for patient use has already been demonstrated in several

* Corresponding author. Department of Nuclear Medicine Saarland University – Medical Center Kirrberger Str. 100, Geb. 50 Homburg, D-66421, Germany.
E-mail address: florian.rosar@uks.eu (F. Rosar).

https://doi.org/10.1016/j.apradiso.2025.112171
Received 26 May 2025; Received in revised form 8 September 2025; Accepted 8 September 2025
Available online 9 September 2025

small cohorts and case studies on both ^{161}Tb-DOTATOC and ^{161}Tb-PSMA (Schaefer-Schuler et al., 2024; Baum et al., 2021; Rosar et al., 2023; Al-Ibraheem et al., 2023; Fricke et al., 2024). As a consequence, the first international prospective studies (e.g., Phase I/II VIOLET study for [^{161}Tb]Tb-PSMA-I&T, Australia, NCT05521412; Phase 0/I BETA PLUS study for [^{161}Tb]Tb-DOTA-LM3, Switzerland, NCT05359146) for the clinical testing of ^{161}Tb-based radiopharmaceuticals have been initiated with the first results having been recently published (Buteau et al., 2025).

However, to enable patient-individual therapy with ^{161}Tb-based radiopharmaceuticals, post-therapeutic scintigraphic imaging of a quality appropriate for dosimetry is essential. This issue also requires absolute quantification of scintigraphic imaging to estimate the activity distribution within a given source region. Post-therapeutic imaging commonly employs both planar and tomographic SPECT techniques, which are both well-established in clinical practice. Although planar scintigraphy is more time-efficient, tomographic SPECT imaging provides three-dimensional data, allowing for more accurate and reliable quantification and is therefore preferable for dosimetry purposes. To obtain accurate SPECT images, it is essential to select a nuclide-specific energy window and an appropriate collimator, and to apply correction methods such as attenuation, scatter, and dead-time correction (if necessary), as well as collimator-detector response modelling. These are generally incorporated into iterative reconstruction and supported by most commercial SPECT/CT systems. However, a camera calibration factor must still be determined to convert the three-dimensional count distribution in the reconstructed images into the activity distribution of the specific radionuclide. This calibration factor (CF) reflects the sensitivity of the camera system for detecting a particular radionuclide and depends on various parameters, such as the energy (and energy window setting) of the measured photons or the collimator used during acquisition. Besides technical considerations, the CF remains ultimately one of the most critical components for reliable activity quantification and subsequent calculations, especially those relating to dosimetry. In addition, to convert the activities calculated e.g. for smaller metastases into absorbed doses, segmentation of the respective volumes within the reconstructed datasets is required. Since the segmented volumes may be influenced by partial volume effects, appropriate corrections, such as recovery coefficient (RC) corrections, must be applied. It could be demonstrated for routinely used radionuclides such as ^{177}Lu, that accurate quantitative calculations are feasible, if the relevant parameters are properly considered (Beauregard et al., 2011; Uribe et al., 2017; Zhao et al., 2018; Ljungberg et al., 2016). However, such evaluations need to be performed for each newly introduced radionuclide to ensure reliable results.

Previously, several phantom studies on preclinical small-animal SPECT/CT systems have successfully demonstrated that the implementation of scintigraphic imaging with ^{161}Tb is feasible (Lehenberger et al., 2011; Müller et al., 2012; Koniar et al., 2024). However, the performance of clinical SPECT/CT systems using ^{161}Tb, e.g. regarding the achievable quantitative accuracy, has scarcely been studied so far (McIntosh et al., 2024; Marin et al., 2020). Marin et al. evaluated the dependence of image quality on energy window setting, choice of collimator and in-house reconstruction methods. This group demonstrated that using a single energy window at 74.6 keV with a low-energy high-resolution collimator yields superior imaging quality compared to a dual energy window technique encompassing both emission peaks (Marin et al., 2020). This result agrees with previous findings on ^{177}Lu, where down-scattering of higher-energy photons into the lower energy window have shown to increase noise levels (Nuttens et al., 2024; Blower et al., 2020). McIntosh et al. focussed on partial volume effect and sensitivity calibration on SPECT imaging with ^{161}Tb, thereby also investigating the effect of dual-energy and triple-energy-window window (DEW and TEW) scatter correction method (McIntosh et al., 2024).

The present study builds upon the results of Marin et al. and McIntosh et al., further investigating the feasibility of quantitative SPECT, hereby focussing on determining the minimum number of counts required to ensure reliable lesion detectability. To allow accurate quantitative imaging with ^{161}Tb, the respective calibration factor of the gamma camera as well as the recovery coefficients were determined and validated by phantom measurements.

2. Material and methods

2.1. Phantom measurements and acquisition protocol

No-carrier-added [^{161}Tb]$TbCl_3$ dissolved in a 0.5 M HCl solution was obtained from Terthera B.V. (Breda, Netherlands) and subsequently chelated by adding DTPA. A NEMA IEC Body phantom with a nominal background volume of 9.6 L and six fillable hollow spheres with inner diameters of 37, 28, 22, 17, 13 and 10 mm (measured volumes by weight: 24.7, 11.7, 5.5, 2.8, 1.05, 0.52 mL) respectively, was used for performance evaluation measurements. The phantom and the spheres were filled with homogeneous solution of [^{161}Tb]Tb-DTPA with a sphere-to-background ratio of 9.3 : 1 (initial activity concentration within the spheres and the background: 2465 kBq/mL and 265 kBq/mL, respectively). Phantom measurements were performed over 9 delayed timepoints realizing targeted phantom activities of 2500 MBq down to 100 MBq. Detailed phantom activities of each scan are presented in the supplements (Table S1). For each of the targeted activities mentioned above five SPECT/CT studies of 120 projections per rotation were performed applying different frame durations ranging from 5 to 25 s per projection. In total $n = 45$ data sets were acquired.

To validate the quantitative imaging setup, a first part of additional measurements was performed using a cylindrical phantom (volume: 6.595 mL) filled with homogeneous activity concentrations of 130 kBq/mL (858 MBq), 76 kBq/mL (466 MBq) and 39 kBq/ml (255 MBq), respectively, while using the acquisition parameter already described above. In total $m = 12$ data sets were acquired. For the second part of validation measurements, an insert comprising four fillable glass spheres of different volume (volumes: 62.3, 33.4, 14.2 and 13.8 mL) was fixed inside the cylindrical phantom (subsequently referred to as 'spheres phantom') and two additional analogous data sets were acquired using the acquisition parameters described above. Here, the background volume and the spheres were filled with homogeneous solution of [^{161}Tb]Tb-DTPA with a sphere-to-background ratio of 9.2 : 1 (initial activity concentration within the spheres and the background 760 kBq/mL and 82 kBq/mL, respectively). With reference to the work of Frezza et al. on ^{177}Lu, all target activities of ^{161}Tb employed for phantom measurements were selected to ensure negligible acquisition dead-time (Frezza et al., 2020).

All phantom measurements were performed on a BrightView XCT SPECT/CT system (Philips, Koninklijke Philips N.V., Netherlands), equipped with a double head gamma camera and a high resolution flat-panel X-ray detector system, which is used in clinical practice at the Saarland University Medical Center (Sowards-Emmerd et al., 2009). Based on previous work of Marin et al. (2020), a low-energy high-resolution (LEHR) collimator was evaluated in this study to characterize ^{161}Tb image quality and its application for quantitative SPECT imaging. A uniformity correction map was created using a flat phantom filled with aqueous solution of [^{161}Tb]Tb-DTPA to reduce artifacts that may occur in reconstructed SPECT images. Such artifacts are known to appear due to collimator response and non-uniformity in the response over the detector surface (Marin et al., 2020). The uniformity correction map was used throughout all SPECT measurements. The energy window was set to the gamma emission of ^{161}Tb at 74.6 keV ± 10 %. CT data were acquired in low-dose technique using an X-ray tube voltage of 120 keV and a tube current of 15 mA as applied in clinical routine. CT data were reconstructed with a soft tissue iterative reconstruction to a slice thickness of 2 mm.

All SPECT datasets were reconstructed using the iterative 3-dimensional ordered-subset expectation maximization (OSEM) algorithm as

implemented by the manufacturer. Based on the recommendation of MIRD, an appropriate number of iterative updates (iterations x subsets) was chosen to ensure a sufficient total number of counts in the reconstructed image for convergence. The data of the IEC phantom were reconstructed using a range of iterations (3, 4, 5, 6) with a fixed preset of 10 subsets. The secondary criterion was to minimize the noise in the reconstructed image to allow reliable interpretation of SPECT data. Stable quantification was achieved with 4 iterations and 10 subsets (corresponding to 40 updates), with the total number of reconstructed counts increasing by less than 0.6 % for higher numbers of updates that was accompanied by a noise increase of approximately 2.5 % for every additional 10 updates. Attenuation correction comprised application of a CT-based workflow also provided by the manufacturer (Bai et al., 2003). In this process, the attenuation factors of the applied X-ray energy were converted to the attenuation factors of the detected gamma emission energy (74.6 keV) and used for correction. Scatter correction was also based on the CT data using the effective source scatter estimation (ESSE) approach and performed as provided by the manufacturer (Frey and Tsui, 1996). The matrix size was 128 × 128, the reconstructed voxel size 4.664 × 4.664 × 4.664 mm^3.

2.2. Performance evaluation

2.2.1. Visual assessment

The performance evaluation included a visual assessment of the image quality of the reconstructed SPECT images carried out by two experienced nuclear medicine physicians and three experienced medical physicists. The criterion evaluated was the detectability of the individual spheres in the reconstructed SPECT slices (transverse, coronal and sagittal slices) and in the maximum intensity projections (MIP) for all phantom measurements. Each reviewer needed to individually assess which of the spheres could be visually distinguished from the background. The mandatory criteria for the clear delineation of a sphere from the background were defined as follows: (i) Identification of the sphere in the MIP from various viewing angles, (ii) Identification of the sphere in at least two consecutive slices (slice thickness 4.664 mm, 128 × 128 matrix) in each of the three orthogonal planes. In the overall rating of the results by all five experts, a sphere was considered clearly detectable if the majority of reviewers (at least three out of five) shared this judgement. All reviewers were blinded to acquisition details while reading the SPECT images. For this analysis, the image viewing software Sectra IDS7 (Sectra AB, Linköping, Sweden) was used by each reviewer. All assessments were performed under standardized accredited viewing conditions consistent with those used in routine clinical interpretation of patient images. Image adjustments (e.g. windowing) were performed individually by each reviewer in the same manner they would typically apply during clinical routine. Inter-observer agreement was assessed by Fleiss' κ (Fleiss, 1971). The respective results were then related to the total number of photopeak counts acquired during measurement.

2.2.2. Quantitative assessment

The reconstructed SPECT/CT data of the different phantoms were analyzed with respect to (i) the image calibration factor (CF) (IEC phantom and cylindrical phantom), (ii) the recovery coefficient (RC) (IEC phantom and spheres phantom) and (iii) the contrast-to-noise ratio (CNR) of the individual spheres (IEC phantom). Volumes of interest (VOI) were defined for each individual sphere, for the background region of the IEC phantom, and for the total volume of both, the IEC and the cylindrical phantom in the reconstructed dataset of each measurement. The total counts and the average counts in the respective VOIs and their standard deviation were used for further evaluation. The VOI segmentation and analysis was performed using PMOD Version 4.3044 (PMOD Technologies LLC, Fällanden, Switzerland) with no additional image post-processing. Contouring of the sphere VOI was performed in two steps. In the first step, a boundary VOI was manually drawn around each sphere encompassing the entire sphere volume to ensure exclusive sphere volume detection. In the second step, the respective sphere VOI was automatically segmented within the boundary using a 50 % isocontour around the sphere-voxel with the maximum count content according to a well-established segmentation method proposed by Boellard et al. (Boellaard et al., 2010). However, in cases of very low contrast, the threshold was manually adjusted by using the respective CT data (fused images as used in clinical practice) to avoid overestimating the sphere volume by more than 10 % and to support accurate VOI placement. For the analysis of the background, eight cuboid, off-center VOIs were defined. Each of these VOIs has a minimum distance of 5 voxels to the nearest sphere and to the outer phantom wall. The volume of each background VOI was approximately 110 mL. The contouring of the total phantom volume was performed analogue to the contouring of the spheres. In the first step, a cuboid VOI was placed as a boundary VOI around the phantom. Then, an isocontour was created with the contoured volume matching the true volume of the phantom.

The image calibration factor CF enables quantitative estimation of the activity distribution of a specified radionuclide, in this study ^{161}Tb, within reconstructed SPECT/CT images. This factor needs to be calculated for each combination of collimator, energy window and reconstruction method as the number of reconstructed counts per Becquerel activity and seconds of acquisition time (counts/Bq*s). In detail, CF is defined as the ratio of the total reconstructed counts N_V of the reference volume V to the respective true activity A_{true} in the reference volume, with A_{true} corrected for the acquisition duration time (the number of projections s multiplied by the acquisition frame time t. In this work, CF was calculated based on the following three different reference volumes: total phantom volume (reference 1), homogenous background (reference 2), and volume of sphere S1 (reference 3). The results were compared with each other.

$$CF_V = \frac{N_V}{A_{V,true} \cdot s \cdot t}$$

The recovery coefficient (RC) quantifies the accuracy of the apparent activity concentrations within the reconstructed SPECT/CT images. The RC was calculated as the ratio of the SPECT/CT-based activity A_{calc} within the sphere S_i of nominal volume V_i and the activity A_{true} known from the initial applied activity concentration. Here, A_{true} needs to be corrected for radioactive decay to the time of the SPECT/CT measurement. The calculation was performed for each measurement and each sphere S_i.

$$RC_S = \frac{A_{S,calc}}{A_{A,true}}$$

The recovery coefficients of the different sphere volumes were fitted to a two-parameter (α and β) model following the recommendations of MIRD (Marquis et al., 2025).

$$RC(V) = \frac{1}{1 + \left(\frac{a}{V}\right)^b}$$

In addition, the inverse recovery coefficients of the different sphere volumes were also calculated. As a first approximation the volume-dependent RC can be applied to correct PVE of the activity concentration within the spheres (Hoffman et al., 1979; Jomaa et al., 2018).

CNR were determined for each sphere S_i and measurement as the difference of the mean number of counts per voxel in the sphere S_i ($\overline{E_S}$) and the background ($\overline{E_{BG}}$), respectively, divided by the mean standard deviation of the mean number of counts in background VOIs (σ_{BG}).

$$CNR = \frac{\overline{E_S} - \overline{E_{BG}}}{\sigma_{BG}}$$

2.3. Case studies from clinical application

SPECT/CT data of two patients after application of [^{161}Tb]Tb-PSMA-617 were acquired applying the clinical standard protocol, which is largely identical with the protocol used for phantom measurements. Solely, to take into account the high physical burden for the patient caused by SPECT/CT examinations, the SPECT frame time was set to 20 s. Reconstruction encompassed attenuation corrected iterative OSEM with 4 iterations and 10 subsets and a Butterworth 0.5 post-processing smoothing filter (Hudson and Larkin, 1994).

2.4. Statistical analysis

The descriptive statistics of the data, such as mean, standard deviation, minimum, and maximum, as well as regression analyses and nonlinear curve fits, were performed using Prism software version 8.2.0 (GraphPad Software Inc., San Diego, USA).

3. Results

Over the range of activities used for the phantom measurements (100 MBq–2500 MBq) total photopeak counts were acquired ranging from approximately 0.31 million to 28.2 million counts. Details are presented in supplementary material (Table S1). Respective count rate calculated by division of the total photopeak counts by the frame time duration and the number of projections is found to linearly increase over the range of activities (compare supplemental data, Fig. S1).

3.1. Visual assessment

The visual analysis of the reconstructed SPECT/CT images revealed different detectability depending on the sphere diameter and the measured photopeak counts. The spheres with diameters S1 (37 mm) and S2 (28 mm) were rated detectable in all 45 measurements (100 %), while the spheres S3 (22 mm), S4 (17 mm), and S5 (13 mm) were rated detectable in only 42 (93.3 %), 33 (73.3 %), and 18 (40.0 %) out of 45 measurements, respectively. In none of the measurements the smallest sphere S6 (10 mm) was rated detectable. Inter-observer agreement was high with a Fleiss' κ of 0.829. A limit value of photopeak counts was determined for each sphere, above which a sphere diameter was rated as detectable in the reconstructed images of each measurement (Fig. 1). This limit value was about 0.98 million, 4.4 million and 11.2 million photopeak counts for spheres S3, S4 and S5, respectively. Moreover, the

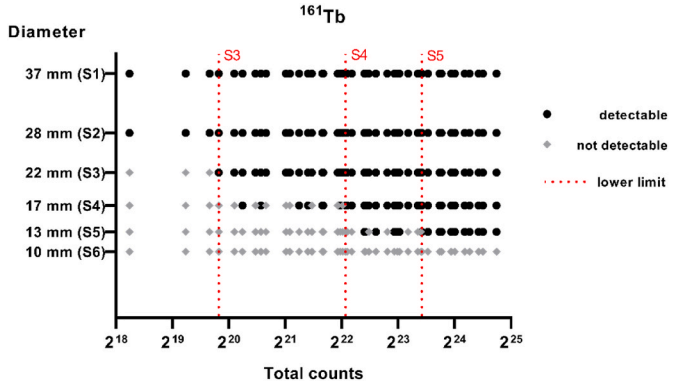

Fig. 1. Results of the visual assessment of sphere detectability. For each sphere, all measurements are displayed over the range of acquired photopeak counts. The lower limit of photopeak counts, above which the respective sphere diameter was consistently rated as detectable, is indicated by a red dashed line. The corresponding limit values were 0.93 million ($2^{19.82}$), 4.4 million ($2^{22.07}$) and 11.2 million counts ($2^{23.42}$) for S3, S4 and S5, respectively. (For interpretation of the references to colour in this figure legend, the reader is referred to the Web version of this article.)

analysis revealed that for each of these spheres there was an additional individual range of acquired photopeak counts lower than the limit value for which the respective sphere was reliably detectable in the reconstructed images, although not in all, but in a certain number of measurements. Fig. 2 shows representative transversal slices from different SPECT/CT measurements with ^{161}Tb, where one of the spheres S2, S3, S4 or S5 was evaluated as the smallest detectable sphere. The effect was linked to the total activity in the phantom which was shown to be proportional to the total acquired statistics and the frame time duration (Table S1, Fig. S1). Exemplarily, for acquiring 1 million counts and thus to enable detectability of S3, of about 100 MBq with 20 s per frame are required. For 5 million counts (detectability of S4), approximately 500 MBq with 20 s per frame are needed, and to acquire 11 million counts (detectability of S5), 1.1 GBq with 20 s per frame are mandatory.

3.2. Quantitative assessment

3.2.1. Calibration factor (CF)

The CF calculated for ^{161}Tb over a wide range of acquired photopeak counts for the three reference volumes of the IEC phantom are shown in Fig. 3A. Only slight differences were observed when using the homogeneous background and total phantom volume of the IEC phantom as references. For photopeak counts higher than 5 million, corresponding to a wide range of applied activity (e.g., >500 MBq, frame time 20 s) the CF was nearly constant with mean values of 12.4 cps/MBq for the total phantom volume and 13.5 cps/MBq for the background. However, an increase in CF was observed when the acquired photopeak counts were reduced to less than 5 million. A nearly constant value of CF was also observed for the third reference volume of the IEC phantom used in this assessment, the volume of sphere S1. However, compared to the other reference volumes significantly lower CF values were obtained for S1 across the entire range of acquired photopeak counts (mean CF: 9.7 cps/MBq acquiring more than 5 million photopeak counts).

For the validation measurements with the cylindrical phantom, CF values were calculated using the total volume as the reference. The corresponding results are presented in Fig. 3B, alongside the respective results obtained for the IEC phantom. For comparison, the CF values calculated for the cylindrical validation phantom agree with those of the IEC phantom within 5 %, with a mean value of 11.8 cps/MBq.

3.2.2. Recovery coefficient

RC values for ^{161}Tb determined for spheres S1 – S5 over the range of acquired photopeak counts are presented in Fig. 4A (additional separate analyses according to the different acquisition frame times are shown in Fig. S2 in the supplement material). The RC for each sphere also remained nearly constant over the range of acquired photopeak counts greater than 5 million with average RC of 0.80 ± 0.02, 0.67 ± 0.04, 0.47 ± 0.02, 0.28 ± 0.02 and 0.22 ± 0.02 for S1 – S5, respectively. However, in combination with reduced acquired photopeak counts, an increase in the RC was observed, accompanied by larger fluctuations. Considering sphere diameter, a decrease in mean RC was observed with decreasing sphere diameter (Fig. 4B).

Recovery curve fitted for the calculated RC of the spheres of the IEC phantom and its 95 % confidence interval are shown in Fig. 5A together with the results of the RC validation analysis (with the spheres phantom). All RC calculated for the spheres of the spheres phantom are within the 95 % confidence interval of the RC curve fit.

The reciprocal mean RC values for all measurements and sphere volumes along with the respective inverse RC-curve are presented in Fig. 5B. These curves should allow for estimation of the true activities of ^{161}Tb in reconstructed SPECT/CT images, particularly for small-volume objects.

3.2.3. Contrast-to-noise ratio (CNR)

CNR for all spheres in reconstructed images increased with

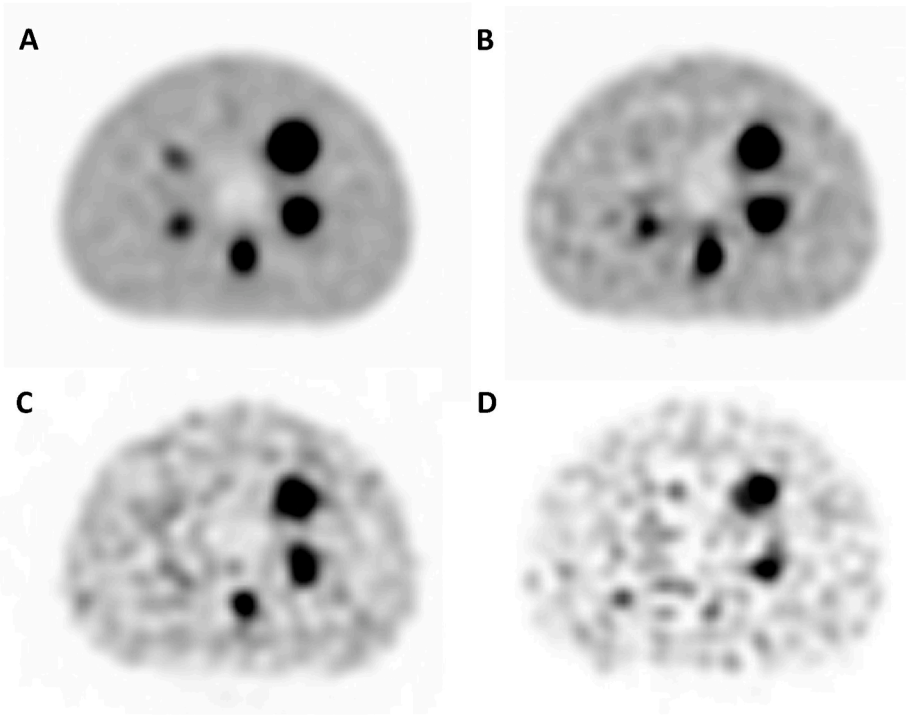

Fig. 2. Representative transversal slices of different SPECT measurements with ^{161}Tb. The smallest visually distinguishable sphere diameter was identified in the different slices as, **A**: the sphere S5 (13 mm), **B:** the sphere S4 (17 mm), **C**: the sphere S3 (22 mm), and **D**: the sphere S2 (28 mm) (photopeak counts acquired, A: 28.0 million B: 7.3 million, C: 1.7 million and D: 0.31 million).

increasing acquired photopeak counts and sphere diameter. Over the range of acquired photopeak counts relatively low CNR values of 2.52–12.06 were determined for the smallest sphere S5 (13 mm diameter), whereas sphere S1 (37 mm diameter) showed a CNR of 11.7 up to 70.6. Fig. 6 summarizes the CNR for all spheres, S1 to S5, in reconstructed images over the range of acquired photopeak counts. In addition, a separate analysis according to the different acquisition frame times is shown in Fig. S3 in the supplement material. In a complementary analysis, the CNR values were also combined with the results of the visual assessment to evaluate the CNR required to ensure detectability of the different spheres S5 (13 mm), S4 (17 mm), and S3 (22 mm), respectively (Fig. S4). The resulting CNR threshold values were 7.10, 7.32 and 7.45 for spheres S5 (13 mm), S4 (17 mm), and S3 (22 mm), respectively.

3.2.4. Case studies from clinical application

Fig. 7 illustrates reconstructed SPECT/CT images of two patients with metastasized, castration-resistant prostate carcinoma who received [^{161}Tb]Tb-PSMA-617 RLT. Case 1 depicts a 65-year-old patient with osseous metastasized prostate carcinoma, while Case 2 features a 76-year-old patient with both osseous and hepatic metastases. 48 h after administration of 6.8 GBq and 5.9 GBq [^{161}Tb]Tb-PSMA-617, respectively, SPECT/CT scans of the abdomen comprised acquisition of 5.3 million and 6.3 million photopeak counts, respectively.

The reconstructed SPECT/CT slices of both patients exhibit typical physiological uptake in the liver, the spleen, the kidneys, and the intestines. In addition, in both cases, pathological structures are clearly delineable. Not only metastases of larger volume, but also small, faintly accumulating metastases can be precisely identified. Exemplarily, for Case 1, Fig. 7A shows a bone metastasis in the spine, approximately 10 mm in size. For Case 2, Fig. 7B demonstrates two hepatic metastases, approximately 20 mm and 10 mm in size and some smaller, faintly accumulating bone metastases in the ribs. For dosimetry purposes, the measured SPECT voxel values were converted to activity using CF and subsequently corrected by applying the corresponding volume-dependent RC. Respective estimated absorbed doses of the normal organs and metastases are presented in the supplemental data (Table S2).

4. Discussion

In this study we have evaluated the performance of a clinical SPECT/CT system for use in post-therapy imaging of ^{161}Tb through phantom measurements, employing both visual assessment and quantitative evaluation. Phantom measurements were performed with a standardized body phantom (NEMA IEC Body Phantom), filled with activities ranging from 2.5 GBq down to 100 MBq, as such values are typically expected in patient scans on the day of injection up to one week after the administration of the radiopharmaceutical. The limit activity was deliberately set very low to investigate whether sufficient image quality can still be achieved and whether quantitative evaluation of measurements is still feasible at such low activities. We could demonstrate that the use of ^{161}Tb can produce high quality SPECT images.

Our results demonstrate that structures up to a diameter of 13 mm could be clearly delineated in reconstructed images with ^{161}Tb, if a certain number of photopeak counts was achieved during measurement. This reliable detection of small spheres with diameters of 13 mm and 17 mm in SPECT imaging with ^{161}Tb required acquisition of a minimum of approximately 11 million and 4.4 million photopeak counts, respectively. Of clinical interest, around 11 million (4.4 million) photopeak counts were acquired during a SPECT with about 1 GBq (500 MBq) of ^{161}Tb and a SPECT frame duration of 20 s. Of note, this individual limit value of photopeak counts for each sphere was not a sharply discrete value, but rather, an additional range of acquired photopeak counts was observed that fell below the threshold, within which the spheres were still frequently considered reliably detectable in the reconstructed image. Structures larger than 22–28 mm, were clearly detectable in any case, even at very low photopeak counts (<0.5 million counts), corresponding to small activities of about 100 MBq.

In this context, it is worth mentioning that the required number of photopeak counts for the detectability of spheres with a diameter of

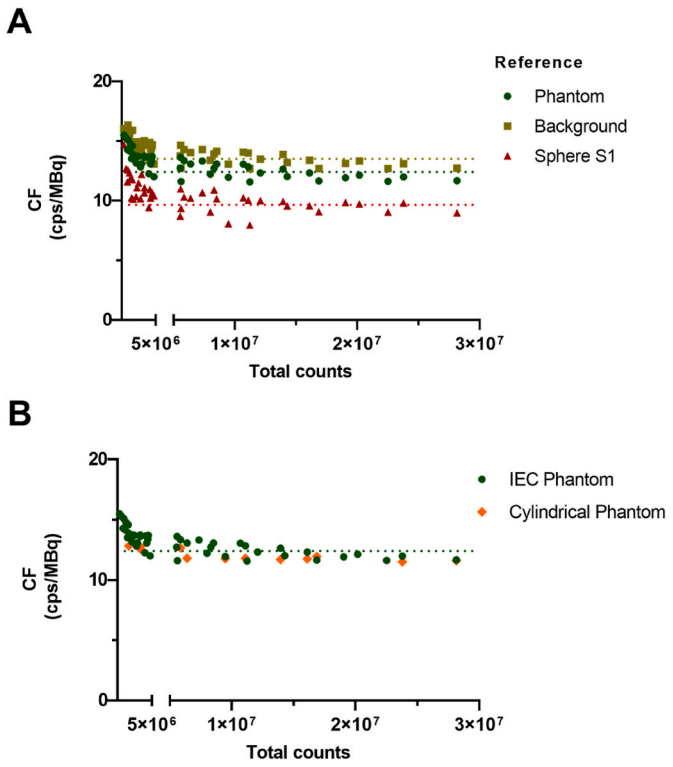

Fig. 3. A: Calibration factor (CF) measured with the IEC phantom for the three reference volumes – total phantom volume (green), background (gold), and sphere S1 (red) over a large range of photopeak counts. Dashed line represents the mean values of CF being nearly constant at photopeak counts larger than 5 million. **B:** Comparison of CF determined for the total volume of the cylindrical phantom (orange) and the IEC phantom, respectively. (For interpretation of the references to colour in this figure legend, the reader is referred to the Web version of this article.)

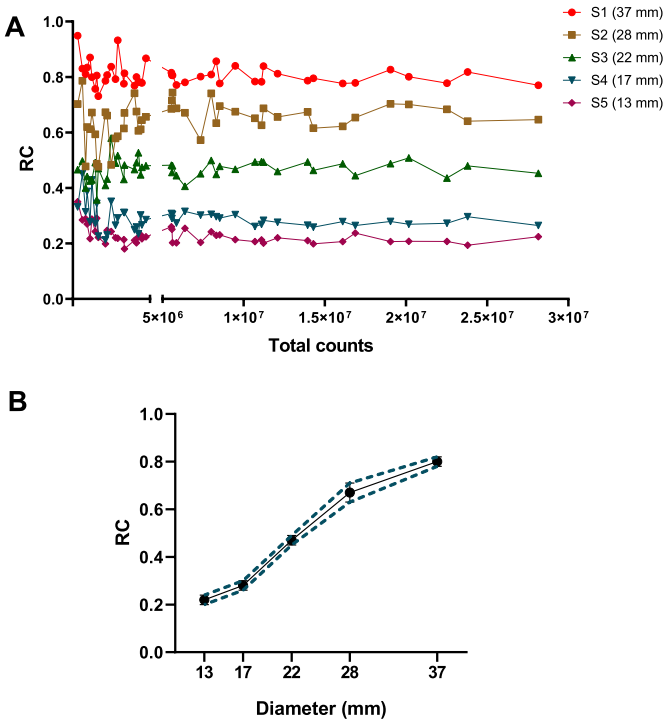

Fig. 4. A: Recovery coefficient (RC) for the spheres S1 – S5 over the range of acquired photopeak counts. **B:** Average RC ± standard deviation over the measurements with >5 million photopeak counts for the different sphere diameter.

≥13 mm largely meets the so-called Rose criterion (visibility at signal-to-noise ratio >5) (Rose, 1948; Burgess, 1999). Interestingly, we observed a required CNR of about 7 to detect the spheres. The slightly higher CNR threshold can be explained by the non-negligible activity in the phantom background and the relatively stringent criterion of reliable detectability.

Recent phantom measurements for SPECT imaging with ^{161}Tb by McIntosh et al. showed similar results to ours (McIntosh et al., 2024). These authors demonstrated that visually acceptable images with clear delineation of sphere diameters of 22 mm and more could be obtained with total activities as low as 300 MBq (McIntosh et al., 2024). Building on this observation, we present an extensive visual assessment that offers comprehensive information on this issue.

In addition, our findings were confirmed by initial patient post-therapeutic imaging. Adequate in-vivo SPECT image quality was achieved 48 h after application of about 6 GBq of [^{161}Tb]Tb-PSMA-617, allowing for reliable interpretation. Metastases of diameter 10–15 mm could be distinctly delineated in the reconstructed images in low background regions. Total counts of 5–7 million are found when examining the count statistics, comparable to those needed to reliably detect spheres of 17 mm diameter in the phantom measurements with relatively high background activity. Consequently, clinical imaging protocols should ensure adherence to the threshold of 5 million counts with acquisition times adjusted according to the count rate. Nevertheless, this should always be viewed as a trade-off, taking into account a reasonable balance between quantitative accuracy, patient burden and logistics.

Dosimetry requires precise, quantitative SPECT reconstructions. However, acquired data is influenced by various physical effects, including among others attenuation and scatter, collimator blurring and partial-volume effects. To obtain truly accurate image data, it is necessary to compensate for these effects during the reconstruction process. Therefore, a detailed protocol for the acquisition and reconstruction of the image data with ^{161}Tb was established beforehand, which accounts for these corrections. In short, solely the higher energy 74.6 keV photopeak counts were acquired because unavoidable artifacts in reconstructed images were reported when using the lower energy photopeak of ^{161}Tb at 48.9 keV. These artifacts are caused by additional X-ray emissions as well as scattered photons of the 74.6 keV emission in the low-energy window (Marin et al., 2020). Reconstruction was performed using the manufacturer-implemented software which includes attenuation and scatter correction. This approach has been shown to be suitable for imaging with several radionuclides (Bai et al., 2003; Frey and Tsui, 1996). Reconstruction parameters were chosen based on studies of Ljungberg et al. with ^{177}Lu which showed that 40 updates are necessary for ^{177}Lu to recover at least 90 % of the activity in various organs (Ljungberg et al., 2016). The internal measurements on ^{161}Tb have confirmed this choice of updates.

All measurements were performed according to this protocol and the system-specific calibration factors (CF) for ^{161}Tb were subsequently determined from the resulting data. For this reason, these CF are only valid when applied in accordance with this protocol. It was observed that the CF values remained constant for photopeak counts greater than 5 million, corresponding to a range of activity commonly observed in routine clinical dosimetric imaging, approximately 500 MBq to 2.5 GBq. In addition, the CF values calculated using the whole phantom volume as reference or the background activity agreed to within 6.7 % (mean 12.4 cps/MBq vs. 13.5 cps/MBq). Such small differences may be caused by statistical fluctuations and both spill-out and spill-in phenomena (Blower et al., 2020). These results highlight that the quantitative analysis of reconstructed slices with ^{161}Tb in clinical routine is feasible over a broad activity range. In addition, these results could also be confirmed by comparison to respective validation measurements which were performed applying the protocol to a cylindrical phantom. The CF

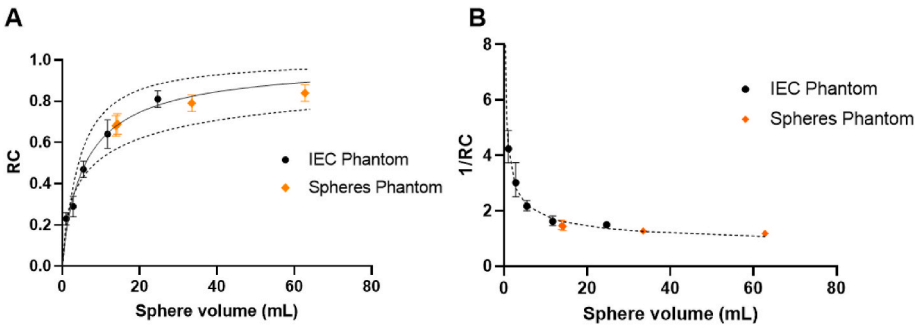

Fig. 5. A: Recovery curves and 95 % confidence intervals fitted using the calculated RC of the spheres of the IEC phantom (black points). RC calculated for the spheres in the validation measurements are also shown (orange diamonds). **B:** Reciprocal volume-based RC curve and reciprocal mean RC values for all measurements and sphere volumes. (For interpretation of the references to colour in this figure legend, the reader is referred to the Web version of this article.)

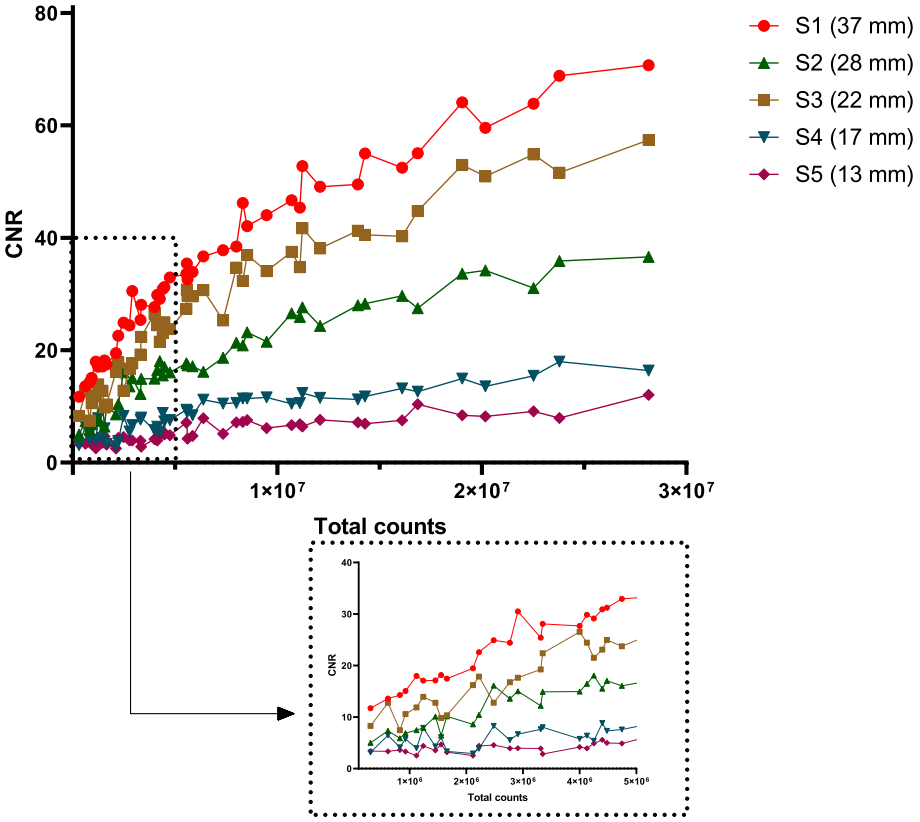

Fig. 6. Contrast-to-noise ratio (CNR) for sphere diameter S1 – S5 over the range of acquired photopeak counts. To highlight the results for low photopeak counts, this range is shown enlarged for better clarity.

values calculated for the cylindrical validation phantom agreed with those obtained from the IEC phantom within 5 %, with a mean value of 11.8 cps/MBq. This result thus demonstrates that consistent CF values for imaging with ^{161}Tb are achievable when following the respective protocol.

However, a noticeable increase towards slightly higher CF values was observed in the very low activity range (<500 MBq), and consequently, at low total photopeak counts (<5 million counts). This increase may be explained by the impact of the low count density within the projection data with ^{161}Tb on the reconstruction process and therefore reduced local count density on the reconstructed image. As the photopeak count rate linearly increases with activity this effect may be caused by an increase in count standard deviation with decreasing activity. Such effects may potentially be further amplified by the reconstruction process, leading to the expected deviation toward lower count rates (Dewaraja et al., 2012). Nevertheless, post-therapeutic imaging at such low activity levels is rather rare in clinical practice and is generally compensated for by an extended acquisition frame time. This phenomenon was also observed and reported for ^{161}Tb by McIntosh et al. for a Siemens Symbia SPECT/CT system (McIntosh et al., 2024). This group additionally reported a clear deviation of acquired photopeak counts from normal distribution at low count density which should have profound impact on the reconstruction process. A constant CF of 14 cps/MBq over a wide range of activity of ^{161}Tb was observed in this study, similar to our own result. Nevertheless, despite the similar values of McIntosh et al. and ours on different systems, it must be emphasized that CF may also vary significantly if site-specific acquisition and reconstruction protocols are used. This was demonstrated in multicenter studies on ^{177}Lu (Tran-Gia et al., 2021; Peters et al., 2020). Exemplarily, the multicenter study of Tran-Gia et al. observed CF values for ^{177}Lu in the range of approximately 10–50 cps/MBq, depending on the SPECT/CT system, the acquisition protocol and the reconstruction

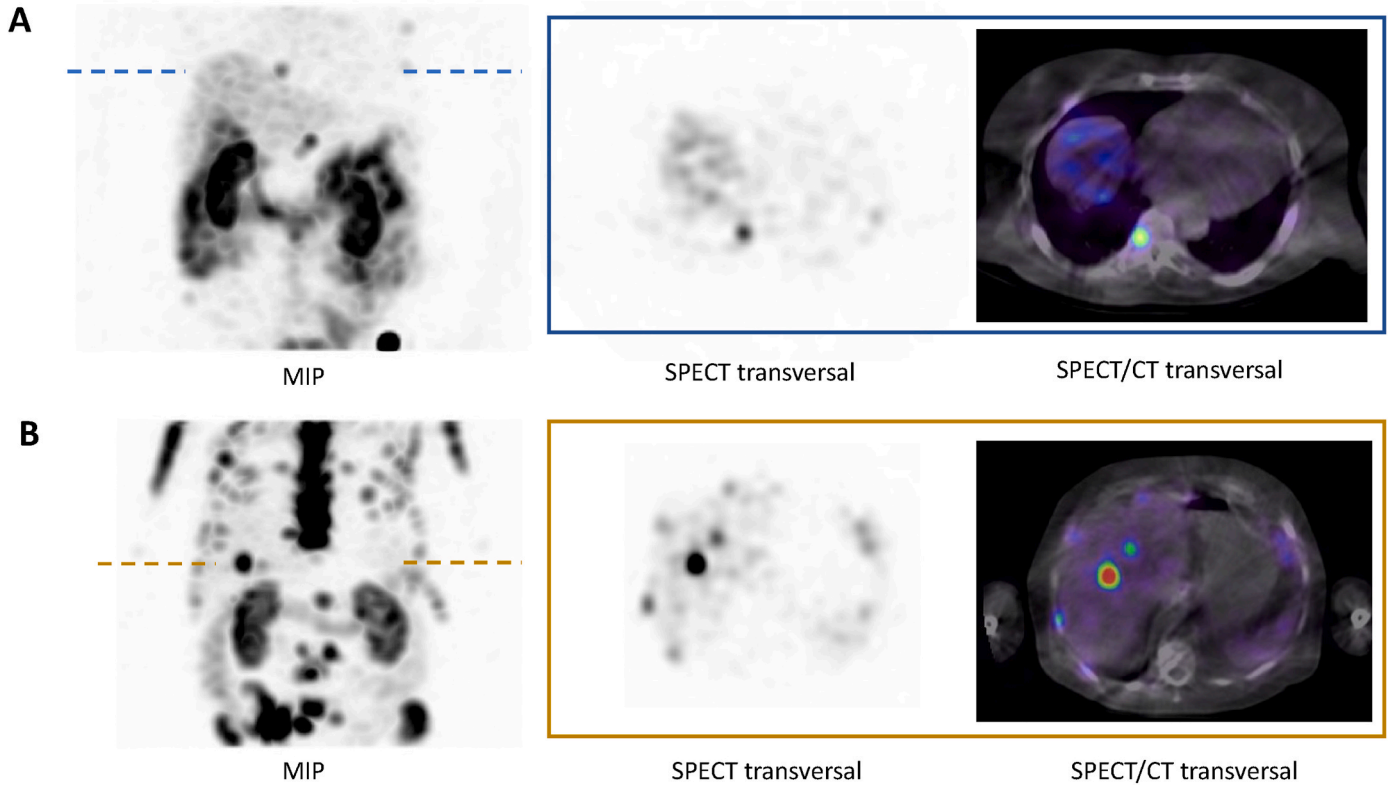

Fig. 7. Maximum Intensity Projection (MIP) and transversal slices of SPECT/CT scans of **A**: a patient with osseous metastasized, castration-resistant prostate carcinoma, 48 h after the administration of 6.8 GBq [^{161}Tb]Tb-PSMA-617 (acquired counts: 5.4 million), which show a bone metastasis in the spine with a diameter of about 10 mm and a tumor-to-background ratio (TBR) of 12.9 and **B**: a patient with osseous and hepatic metastasized, castration-resistant prostate carcinoma, 48 h after the administration of 5.9 GBq [^{161}Tb]Tb-PSMA-617 (acquired counts: 6.3 million). The slices show two hepatic metastases with diameters of about 20 mm (TBR of 78.6) and 10 mm (TBR of 20.9) and some bone metastases of smaller size (TBR up to 19.0).

software used (Tran-Gia et al., 2021). As the primary source of differing CF the reconstruction process was identified including the scatter and attenuation corrections applied. These authors were also able to show that when using similar combinations of imaging system and reconstruction the CF of the individual centers were largely consistent. Consequently, to be able to use ^{161}Tb in clinical trials in the future, including dosimetry studies, comparability of the dosimetry results between different centers needs to be achieved. Thus, future work should focus on reconstruction parameters and their impact on quantitative imaging with ^{161}Tb.

Quantitative accuracy of the apparent activity concentrations within reconstructed SPECT/CT images is highly influenced by partial volume effect (Ljungberg et al., 2016; McIntosh et al., 2024; Marin et al., 2020; Dewaraja et al., 2012). Thus, CF values determined for sphere S1 were expected to be significantly lower (by 21.8–28.1 %, mean 9.7 cps/MBq) as those obtained from the total phantom volume and the background. To compensate for this phenomenon, RC values are commonly used in dosimetry calculations as they allow for estimating true activity concentrations more accurately from the apparent activities measured in quantitative SPECT, especially in small metastases. A volume-based recovery curve and its inverse were determined by regression analysis and subsequently validated through phantom measurements using different phantom geometry. In the context of partial volume correction, correcting the CF of sphere S1 using the recovery curve yields values comparable to the CF determined from the other two references. However, it is important to note, that these results are, in turn, valid for photopeak counts $\geq$5 million. With decreasing photopeak counts (<5 million) and consequently in the lower activity range, deviations and fluctuation of RC for all spheres are observed. Again, this effect should be explained by the low count density and the high standard deviation of counts relative to the mean of the region that may have distinct impact on reconstruction results.

Previous work on ^{161}Tb by Marin et al. and McIntosh et al., respectively, also revealed variations in RC values (RC range: 0.5 and 0.7 for spheres larger than 30 mm in diameter) (McIntosh et al., 2024; Marin et al., 2020). This was expected as currently those results are highly site-dependent with each site using its individual combination of SPECT system, acquisition protocol and reconstruction algorithm. Multicenter studies on SPECT-quantification with ^{177}Lu by Peters et al. and by Tran-Gia et al. consistently demonstrated inter-system variations in RC (Tran-Gia et al., 2021; Peters et al., 2020). Tran-Gia et al. further demonstrated that harmonization among centers can be achieved for ^{177}Lu (Tran-Gia et al., 2021), a successful approach that encourages pursuing similar collaborative efforts in future research on SPECT/CT with ^{161}Tb.

The results of this study should be interpreted in light of certain limitations. Preliminary examination addressing the choice of reconstruction parameters were carried out; nonetheless, a thorough investigation into the selection of appropriate reconstruction settings for ^{161}Tb, especially including the use of advanced correction algorithms (e.g. resolution recovery), should be addressed in subsequent studies. Advanced AI-based algorithms for partial volume correction, as recently proposed for use with ^{177}Lu (Leube et al., 2024; Liu et al., 2024), should also be evaluated for ^{161}Tb. Furthermore, the definition of the VOI may influence the obtained values, particularly the RC. Therefore, complementary VOI strategies such as background-adapted thresholding or fixed-size VOIs should be considered in future studies with ^{161}Tb. Moreover, as this study involved only two patients, patient-specific dosimetry studies in larger cohorts taking our results into account are necessary.

5. Conclusion

The results observed in this study demonstrate that quantitative SPECT/CT imaging with ^{161}Tb is feasible over a wide range of activity making this radionuclide suitable for clinical applications. Acquiring a total of at least 5 million photopeak counts enables visual detectability of lesions of diameter lower than 20 mm and quantitative calibration for dosimetry purposes.

CRediT authorship contribution statement

Florian Rosar: Writing – original draft, Visualization, Methodology, Investigation, Formal analysis, Data curation, Conceptualization. **Sven Petto:** Investigation, Formal analysis. **Sebastian Ganz:** Investigation, Formal analysis. **Caroline Burgard:** Investigation, Formal analysis. **Stephan Maus:** Resources, Investigation. **Mark Bartholomä:** Writing – review & editing, Resources. **Isabelle Miederer:** Resources, Methodology. **Mathias Schreckenberger:** Writing – review & editing, Resources. **Samer Ezziddin:** Writing – review & editing, Resources, Conceptualization. **Andrea Schaefer-Schuler:** Writing – original draft, Methodology, Investigation, Formal analysis, Data curation, Conceptualization.

Availability of data and materials

The datasets used and analyzed during the current study are available from the corresponding author on reasonable request.

Ethics approval and consent to participate

Not applicable.

Consent for publication

Not applicable.

Funding

Nothing to disclose.

Declaration of competing interest

The authors declare that they have no known competing financial interests or personal relationships that could have appeared to influence the work reported in this paper.

Acknowledgements

Not applicable.

Appendix A. Supplementary data

Supplementary data to this article can be found online at https://doi.org/10.1016/j.apradiso.2025.112171.

Data availability

Data will be made available on request.

References

Al-Ibraheem, A., Scott, A.M., 2023. 161Tb-PSMA unleashed: a promising new player in the theranostics of prostate cancer. Nucl Med Mol Imaging 57, 168–171.
Al-Ibraheem, A., Doudeen, R.M., Juaidi, D., Abufara, A., Maus, S., 2023. ^{161}Tb-PSMA radioligand therapy: first-in-humans SPECT/CT imaging. J. Nucl. Med. 64, 1322–1323.
Alcocer-Ávila, M.E., Ferreira, A., Quinto, M.A., Morgat, C., Hindié, E., Champion, C., 2020. Radiation doses from ^{161}Tb and ^{177}Lu in single tumour cells and micrometastases. EJNMMI Phys 7, 33.
Bai, C., Shao, L., Da Silva, A.J., Zhao, Z., 2003. A generalized model for the conversion from CT numbers to linear attenuation coefficients. IEEE Trans. Nucl. Sci. 50, 1510–1515.
Baum, R.P., Singh, A., Kulkarni, H.R., Bernhardt, P., Rydén, T., Schuchardt, C., et al., 2021. First-in-Humans application of ^{161}Tb: A Feasibility Study Using ^{161}Tb-DOTATOC. J. Nucl. Med. 62, 1391–1397.
Beauregard, J.-M., Hofman, M.S., Pereira, J.M., Eu, P., Hicks, R.J., 2011. Quantitative ^{177}Lu SPECT (QSPECT) imaging using a commercially available SPECT/CT system. Cancer Imaging 11, 56–66.
Blower, J.E., Bordoloi, J.K., Rigby, A., Farleigh, M., Kim, J., O'Brien, H., et al., 2020. Protocols for dual tracer PET/SPECT preclinical imaging. Front. Physiol. 8, 126.
Boellaard, R., O'Doherty, M.J., Weber, W.A., Mottaghy, F.M., Lonsdale, M.N., Stroobants, S.G., et al., 2010. FDG PET and PET/CT: EANM procedure guidelines for tumour PET imaging: version 1.0. Eur. J. Nucl. Med. Mol. Imag. 37, 181–200.
Borgna, F., Haller, S., Rodriguez, J.M.M., Ginj, M., Grundler, P.V., Zeevaart, J.R., et al., 2022. Combination of terbium-161 with somatostatin receptor antagonists-a potential paradigm shift for the treatment of neuroendocrine neoplasms. Eur. J. Nucl. Med. Mol. Imag. 49, 1113–1126.
Burgess, A.E., 1999. The rose model, revisited. J. Opt. Soc. Am. Opt Image Sci. Vis. 16, 633–646.
Buteau, J.P., Kostos, L., Jackson, P.A., Xie, J., Haskali, M.B., Alipour, R., et al., 2025. First-in-human results of terbium-161 [^{161}Tb]Tb-PSMA-I&T dual beta-Auger radioligand therapy in patients with metastatic castration-resistant prostate cancer (VIOLET): a single-centre, single-arm, phase 1/2 study. Lancet Oncol. 26, 1009–1017.
Champion, C., Quinto, M.A., Morgat, C., Zanotti-Fregonara, P., Hindié, E., 2016. Comparison between three promising ß-emitting radionuclides, ^{67}Cu, ^{47}Sc and ^{161}Tb, with Emphasis on Doses Delivered to Minimal Residual Disease. Theranostics 6, 1611–1618.
Dewaraja, Y.K., Frey, E.C., Sgouros, G., Brill, A.B., Roberson, P., Zanzonico, P.B., et al., 2012. MIRD pamphlet No. 23: quantitative SPECT for patient-specific 3-dimensional dosimetry in internal radionuclide therapy. J. Nucl. Med. 53, 1310–1325.
Fleiss, J., 1971. Measuring nominal scale agreement among many raters. Psychol. Bull. 76, 378.
Frey, E.C., Tsui, B.M.W., 1996. A new method for modeling the spatially-variant, object-dependent scatter response function in SPECT. IEEE Nucl Sci Symp Conf Rec. 1996 2, 1082–1086.
Frezza, A., Desport, C., Uribe, C., Zhao, W., Celler, A., Després, P., et al., 2020. Comprehensive SPECT/CT system characterization and calibration for ^{177}Lu quantitative SPECT (QSPECT) with dead-time correction. EJNMMI Phys. 7, 10.
Fricke, J., Westerbergh, F., McDougall, L., Favaretto, C., Christ, E., Nicolas, G.P., et al., 2024. First-in-human administration of terbium-161-labelled somatostatin receptor subtype 2 antagonist ([^{161}Tb]Tb-DOTA-LM3) in a patient with a metastatic neuroendocrine tumour of the ileum. Eur. J. Nucl. Med. Mol. Imag. 51, 2517–2519.
Grünberg, J., Lindenblatt, D., Dorrer, H., Cohrs, S., Zhernosekov, K., Köster, U., et al., 2014. Anti-L1CAM radioimmunotherapy is more effective with the radiolanthanide terbium-161 compared to lutetium-177 in an ovarian cancer model. Eur. J. Nucl. Med. Mol. Imag. 41, 1907–1915.
Hindié, E., Zanotti-Fregonara, P., Quinto, M.A., Morgat, C., Champion, C., 2016. Dose deposits from ^{90}Y, ^{177}Lu, ^{111}In, and ^{161}Tb in Micrometastases of Various Sizes: Tmplications for Radiopharmaceutical Therapy. J. Nucl. Med. 57, 759–769.
Hoffman, E.J., Huang, S.C., Phelps, M.E., 1979. Quantitation in positron emission computed tomography: 1. Effect of object size. J. Comput. Assist. Tomogr. 3, 299–308.
Hudson, H.M., Larkin, R.S., 1994. Accelerated image reconstruction using ordered subsets of projection data. IEEE Trans. Med. Imag. 13, 601–609.
Jomaa, H., Mabrouk, R., Khlifa, N., 2018. Post-reconstruction-based partial volume correction methods: a comprehensive review. Biomed. Signal Process Control 46, 131–144.
Koniar, H., McNeil, S., Wharton, L., Ingham, A., Van de Voorde, M., Ooms, M., et al., 2024. Quantitative SPECT imaging of ^{155}Tb and ^{161}Tb for preclinical theranostic radiopharmaceutical development. EJNMMI Phys 11, 77.
Kratochwil, C., Fendler, W.P., Eiber, M., Hofman, M.S., Emmett, L., Calais, J., et al., 2023. Joint EANM/SNMMI procedure guideline for the use of ^{177}Lu-labeled PSMA-targeted radioligand-therapy (^{177}Lu-PSMA-RLT). Eur. J. Nucl. Med. Mol. Imag. 50, 2830–2845.
Lehenberger, S., Barkhausen, C., Cohrs, S., Fischer, E., Grünberg, J., Hohn, A., et al., 2011. The low-energy β$^-$ and electron emitter ^{161}Tb as an alternative to ^{177}Lu for targeted radionuclide therapy. Nucl. Med. Biol. 38, 917–924.
Leube, J., Gustafsson, J., Lassmann, M., Salas-Ramirez, M., Tran-Gia, J., 2024. A deep-learning-based partial-volume correction method for quantitative ^{177}Lu SPECT/CT Imaging. J Nucl Med Off Publ Soc Nucl Med. 65, 980–987.
Liu, Y., Lu, Z., Chen, G., Shi, K., Mok, G.S.P., 2024. Partial volume correction for Lu-177-PSMA SPECT. EJNMMI Phys 11, 93.
Ljungberg, M., Celler, A., Konijnenberg, M.W., Eckerman, K.F., Dewaraja, Y.K., Sjögreen-Gleisner, K., 2016. MIRD pamphlet No. 26: joint EANM/MIRD Guidelines for quantitative ^{177}Lu SPECT Applied for dosimetry of radiopharmaceutical therapy. J. Nucl. Med. 57, 151–162.
Love, C., Desai, N.B., Abraham, T., Banks, K.P., Bodei, L., Boike, T., et al., 2022. ACR-ACNM-ASTRO-SNMMI practice parameter for Lutetium-177 (Lu-177) DOTATATE therapy. Clin. Nucl. Med. 47, 503–511.

Marin, I., Rydèn, T., Van Essen, M., Svensson, J., Gracheva, N., Köster, U., et al., 2020. Establishment of a clinical SPECT/CT protocol for imaging of ^{161}Tb. EJNMMI Phys 7, 45.

Marquis, H., Schmidtlein, C.R., de Nijs, R., Mínguez Gabiña, P., Gustafsson, J., Kayal, G., et al., 2025. MIRD pamphlet no. 32: a MIRD recovery coefficient model for resolution characterization and shape-specific partial-volume correction. J Nucl Med Off Publ Soc Nucl Med. 66, 457–465.

McIntosh, L., Jackson, P., Emmerson, B., Buteau, J.P., Alipour, R., Kong, G., et al., 2024. Quantitative calibration of Tb-161 SPECT/CT in view of personalised dosimetry assessment studies. EJNMMI Phys. 11, 18.

Müller, C., Zhernosekov, K., Köster, U., Johnston, K., Dorrer, H., Hohn, A., et al., 2012. A unique matched quadruplet of terbium radioisotopes for PET and SPECT and for α^- and β^--Radionuclide therapy: an in vivo proof-of-concept Study with a new receptor-targeted folate derivative. J. Nucl. Med. 53, 1951–1959.

Müller, C., Reber, J., Haller, S., Dorrer, H., Bernhardt, P., Zhernosekov, K., et al., 2014. Direct in vitro and in vivo comparison of ^{161}Tb and ^{177}Lu using a tumour-targeting folate conjugate. Eur. J. Nucl. Med. Mol. Imag. 41, 476–485.

Müller, C., Umbricht, C.A., Gracheva, N., Tschan, V.J., Pellegrini, G., Bernhardt, P., et al., 2019. Terbium-161 for PSMA-targeted radionuclide therapy of prostate cancer. Eur. J. Nucl. Med. Mol. Imag. 46, 1919–1930.

Müller, C., van der Meulen, N.P., Schibli, R., 2023. Opportunities and potential challenges of using terbium-161 for targeted radionuclide therapy in clinics. Eur. J. Nucl. Med. Mol. Imag. 50, 3181–3184.

Nuttens, V., Schramm, G., D'Asseler, Y., Koole, M., 2024. Comparison of a 3D CZT and conventional SPECT/CT system for quantitative Lu-177 SPECT imaging. EJNMMI Phys 11, 29.

Peters, S.M.B., Meyer Viol, S.L., van der Werf, N.R., de Jong, N., van Velden, F.H.P., Meeuwis, A., et al., 2020. Variability in lutetium-177 SPECT quantification between different state-of-the-art SPECT/CT systems. EJNMMI Phys 7, 9.

Reubi, J.C., Schär, J.C., Waser, B., Wenger, S., Heppeler, A., Schmitt, J.S., et al., 2000. Affinity profiles for human somatostatin receptor subtypes SST1-SST5 of somatostatin radiotracers selected for scintigraphic and radiotherapeutic use. Eur. J. Nucl. Med. 27, 273–282.

Rosar, F., Maus, S., Schaefer-Schuler, A., Burgard, C., Khreish, F., Ezziddin, S., 2023. New Horizons in radioligand therapy: ^{161}Tb-PSMA-617 in Advanced mCRPC. Clin. Nucl. Med. 48, 433–434.

Rose, A., 1948. The sensitivity performance of the human eye on an absolute scale. J. Opt. Soc. Am. 38, 196–208.

Sartor, O., de Bono, J., Chi, K.N., Fizazi, K., Herrmann, K., Rahbar, K., et al., 2021. Lutetium-177-PSMA-617 for metastatic castration-resistant prostate cancer. N. Engl. J. Med. 385, 1091–1103.

Schaefer-Schuler, A., Burgard, C., Blickle, A., Maus, S., Petrescu, C., Petto, S., et al., 2024. [^{161}Tb]Tb-PSMA-617 radioligand therapy in patients with mCRPC: preliminary dosimetry results and intra-individual head-to-head comparison to [^{177}Lu]Lu-PSMA-617. Theranostics 14, 1829–1840.

Sowards-Emmerd, D., Balakrishnan, K., Wiener, J., Shao, L., Ye, J., 2009. CBCT-Subsystem Performance of the Multi-Modality Brightview XCT System, p. 3058.

Strosberg, J., El-Haddad, G., Wolin, E., Hendifar, A., Yao, J., Chasen, B., et al., 2017. Phase 3 trial of ^{177}Lu-Dotatate for Midgut Neuroendocrine numors. N. Engl. J. Med. 376, 125–135.

Tran-Gia, J., Denis-Bacelar, A.M., Ferreira, K.M., Robinson, A.P., Calvert, N., Fenwick, A. J., et al., 2021. A multicentre and multi-national evaluation of the accuracy of quantitative Lu-177 SPECT/CT imaging performed within the MRTDosimetry project. EJNMMI Phys 8, 55.

Uribe, C.F., Esquinas, P.L., Tanguay, J., Gonzalez, M., Gaudin, E., Beauregard, J.-M., et al., 2017. Accuracy of ^{177}Lu activity quantification in SPECT imaging: a phantom study. EJNMMI Phys 4, 2.

Verburg, F.A., de Blois, E., Koolen, S., Konijnenberg, M.W., 2023. Replacing Lu-177 with Tb-161 in DOTA-TATE and PSMA-617 therapy: potential dosimetric implications for activity selection. EJNMMI Phys 10, 69.

Zhao, W., Esquinas, P.L., Hou, X., Uribe, C.F., Gonzalez, M., Beauregard, J.-M., et al., 2018. Determination of gamma camera calibration factors for quantitation of therapeutic radioisotopes. EJNMMI Phys. 5, 8.